AGU PUBLICATIONS

JGR

Journal of Geophysical Research: Atmospheres

RESEARCH ARTICLE

10.1002/2015JD024243

Key Points:
- An empirical L_2 model in surface pressure is derived from 2315 globally distributed barometers
- The model attests to the accuracy of L_2 in ERA-Interim, but local ocean tide artifacts exist
- The lunar tide in reanalysis systems is directly linked to the assimilation of in situ pressure data

Supporting Information:
- Figures S1–S6

Correspondence to:
M. Schindelegger,
michael.schindelegger@tuwien.ac.at

Citation:
Schindelegger, M., and H. Dobslaw (2016), A global ground truth view of the lunar air pressure tide L_2, *J. Geophys. Res. Atmos.*, *121*, 95–110, doi:10.1002/2015JD024243.

Received 21 SEP 2015
Accepted 4 DEC 2015
Accepted article online 14 DEC 2015
Published online 7 JAN 2016

A global ground truth view of the lunar air pressure tide L_2

Michael Schindelegger[1] and Henryk Dobslaw[2]

[1]Department of Geodesy and Geoinformation, TU Wien, Vienna, Austria, [2]Deutsches GeoForschungsZentrum (GFZ), Potsdam, Germany

Abstract A comprehensive model of the lunar air pressure tide L_2 is developed on the basis of 2315 ground truth estimates from land barometers and moored buoys. Regional-scale features of the tide and its seasonal modulations are well resolved by the in situ scatter and gridded to a 2° mesh through multiquadric interpolation. The resulting climatologies serve as an independent standard to validate the lunar semidiurnal tidal signal that is present in ERA-Interim reanalysis products despite the absence of L_2-related gravitational forcing mechanisms in the prescribed model physics. Inconsistencies between the reanalysis solution of the barometric lunar tide and its empirical account are generally small, yet when averaged over the period 1979–2010, ERA-Interim underestimates the 100 μbar open ocean tidal amplitude in the Tropics by up to 20 μbar and produces times of peak pressure that are too early by 10 lunar minutes. Large-amplitude features of the reanalysis tide off the coast of Alaska, the eastern U.S., and Great Britain are evidently spurious, introduced to the analysis system by assimilating marine pressure data at an invariant reference surface instead of properly accounting for vertical sensor movements associated with the M_2 ocean tide. Additionally, a credible L_2 signal is documented for the ERA-20C pilot reanalysis of the twentieth century. The fact that this model rests upon input data from mere surface observations provides an unambiguous indication that the lunar tidal oscillation in atmospheric analysis systems is closely tied to the assimilation of conventional pressure measurements from stations and marine objects.

1. Introduction

Tides in the atmosphere go along with the rotation of the Earth within the fields of solar radiation and gravitational attraction from external bodies such as the Moon [*Chapman and Lindzen*, 1970]. *Newton* [1687] correctly anticipated the smallness of gravitationally driven air tides of which early observational evidence was provided in the middle nineteenth century by a barometric determination of the lunar semidiurnal tidal oscillation L_2 at the island of St. Helena [*Sabine*, 1847; *Cartwright*, 1999]. This tide — usually called M_2 following the Doodson convention — corresponds to the strongest partial line of the tidal potential acting on the Earth. The forces imposed on the atmosphere are very well known, comprising both the primary gravitational potential as well as secondary effects related to tidal deformations and mass displacements in other components of the Earth system. In the past, the tide has been a prominent test case for atmospheric model development [e.g., *Stening et al.*, 1997]. Further, the so-called Pekeris resonance peak frequency [*Platzman*, 1988] of the atmosphere is located in the vicinity of the lunar semidiurnal tide, thereby causing strong amplifications of tidal signals in the ionosphere, in particular on the occasion of major stratospheric warming events [*Forbes and Zhang*, 2012; *Forbes et al.*, 2013]. Finally, semidiurnal signals in the atmosphere are of interest for the processing of satellite gravimetry observations from the GRACE (Gravity Recovery and Climate Experiment) mission [*Tapley et al.*, 2004]. A proper reduction of tidal effects can avoid temporal aliasing of high-frequency mass variability into global gravity fields that are typically derived from data accumulated over several days.

In a recent paper, *Kohyama and Wallace* [2014] analyzed the characteristics of the lunar gravitational tide in the ECMWF (European Centre for Medium-Range Weather Forecasts) reanalysis ERA-Interim [*Dee et al.*, 2011] and found plausible pressure level oscillations that are persistent throughout the whole reanalysis period 1979–2011. Contrasting to such broadband assimilative global numerical models, the global structure of L_2 has, however, traditionally been inferred from dedicated, data-free tidal simulations [*Hollingsworth*, 1971; *Vial and Forbes*, 1994; *Pedatella et al.*, 2012]. These studies unanimously agree that several different forcing mechanisms are important for reproducing L_2: (i) the periodic time variations of the tidal potential of the Moon, (ii) secondary gravitational effects due to mass displacements and crustal loading deformations associated with Earth and ocean tides at the very same frequency, and (iii) vertical displacements of the lower

atmospheric boundary that also imply periodic changes in the surface geopotential. Since none of those processes are explicitly included in the ECMWF numerical weather prediction model [*Janssen*, 1999], it is imperative to assess whether the lunar tidal signal in ERA-Interim is reliable and to what extent it is affected by limitations in the analysis system.

This study approaches such a validation from a pure surface pressure perspective. We utilize L_2 determinations from globally distributed barometers that supply the most accurate observational constraints on atmospheric tidal variability at the Earth's surface even today. In situ compilations of that kind have been previously assembled and mapped to a global domain by *Haurwitz and Cowley* [1969] as well as by *Goulter* [2005], involving some 100 individually analyzed stations from which only the continental-scale features of the tide could be inferred. Here a new ground truth data set of more than 2000 pressure tide estimates is developed in an attempt to advance our knowledge of L_2 at ground level and check the fidelity of its representation in ERA-Interim. We tidally analyze station-wise synoptic pressure observations from the Integrated Surface Database (ISD) [*Smith et al.*, 2011] over a 110 year period and optimize the spatial coverage of this compilation with station and buoy data from other archives. The resulting in situ scatter is gridded to a 2° mesh through objective interpolation with radial basis functions, and the deduced global climatologies of L_2 are subsequently compared over a nominal analysis window from 1979 to 2010 to the tidal signals within ERA-Interim as well as ERA-20C [*Poli et al.*, 2013], a more recent reanalysis of the ECMWF. This validation primarily focuses on the more robust annual mean signal, but, to the extent possible, seasonal variations of the tide are also taken into account.

The joint consideration of barometric data from both land-based and marine sensors as well as the obvious limitations of numerical weather prediction models in representing the lunar tide have prompted the inclusion of section 2, where we specify the different systematics in the local barometric L_2 signal related to vertical shifting of the crust and the ocean surface. Section 3 provides details on our tidal analysis and outlines the algorithms employed to arrive at an internally consistent pressure tide compilation. We compare our empirical L_2 model to the corresponding climatologies from atmospheric reanalyses in section 4 and also demonstrate that the tidal signal in these assimilation systems is closely related to the meteorological input data (section 5). Finally, implications for potential lunar tidal applications are discussed in section 6.

Throughout this paper we understand the semidiurnal lunar frequency to correspond to a period half the lunar day (i.e., 12.42 h). Following conventional terminologies, tidal oscillations of this frequency will be designated as M_2 for the case of the oceans and as L_2 for the atmospheric response to the principal gravitational forcing.

2. L_2 and Planetary Tidal Deformations

The gravitational lunar tide in the Earth system involves oscillations of the oceans, the atmosphere, and the solid parts of our planet. Hence, the tidal signals recorded by barometers attached to the interfaces of these subsystems not only represent the dynamic component of the lunar tide in the atmosphere but are also manifestations of the vertical sensor motion due to the body tide, the ocean tide, as well as corresponding secondary loading effects. In the following, we briefly discuss these contributions to the pressure tide in ground truth data and select a proper reference surface for our L_2 determinations. We are led by the notion of oceanography that reckons tides with respect to the vertically displaced lower boundary layer (i.e., the seabed). Accordingly, tides in the atmosphere are perceived as the variation in air mass above the vertically moving crust or the sea surface.

The closed-form expression of the body tide for radial displacements ζ at the lunar tidal frequency ω given in *Petit and Luzum* [2010] is adequately approximated by

$$\zeta \approx [14.7\ \text{cm}] \cos^2 \varphi \cos(\omega\tau + 2\lambda), \tag{1}$$

where φ is latitude, λ denotes longitude, and τ is time reckoned from the passage of the Moon through the Greenwich (or 180°) meridian. Disregarding a small phase lag of 0.2° [*Ray et al.*, 2001], the body tide follows the perturbing M_2 astronomical potential in the manner of an instantaneous equilibrium response. This signal translates to a pressure variation of

$$-\rho_0 g\zeta \approx -\left[17.6\ \mu\text{bar}\right] \cos^2 \varphi \cos(\omega\tau + 2\lambda) \tag{2}$$

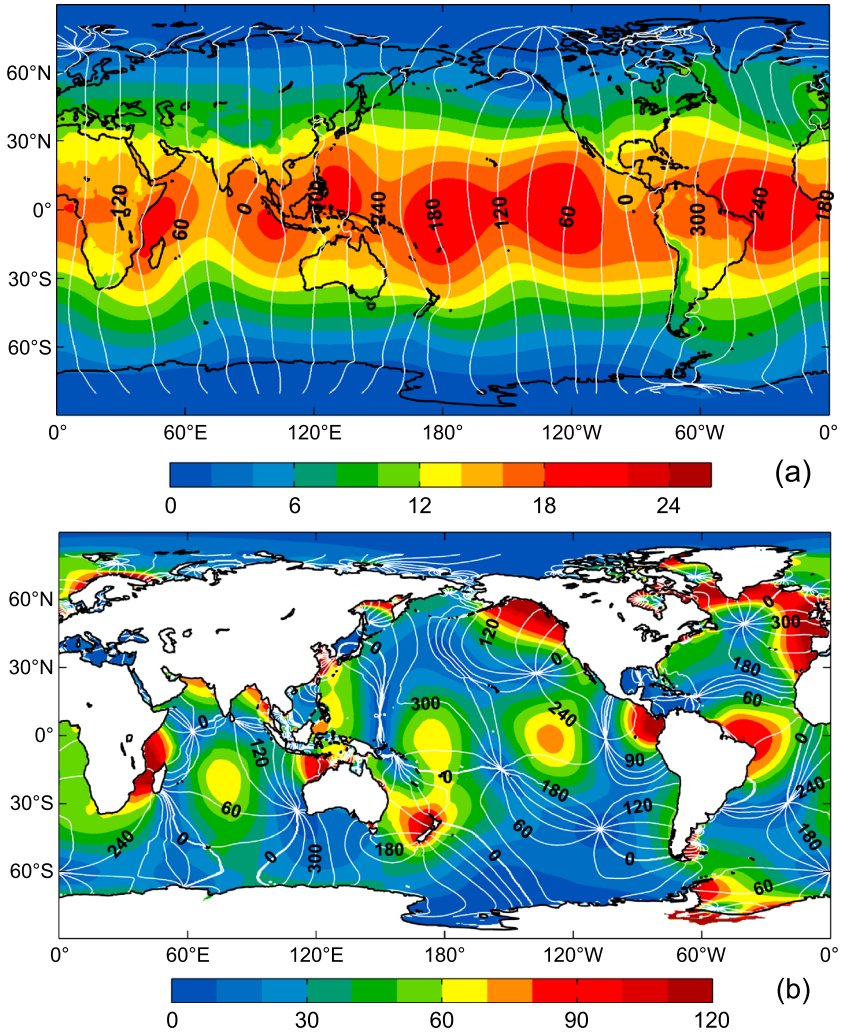

Figure 1. (a) Cotidal chart of the body + ocean load tide contribution to L_2 for barometers attached to the Earth's crust, with the loading displacement field inferred from FES2012. The solid Earth tide correction $-\rho_0 g\zeta = -[17.6\ \mu\text{bar}]\cos^2\varphi\cos(\omega t + 2\lambda)$ is virtually out of phase with the air tide. Color-filled contours show amplitudes in μbar, and white isolines indicate Greenwich phase lag every 30°. (b) Amplitudes (μbar) and phase lags of δp_{M_2}, the static contribution of the ocean tide to the barometric L_2 tide as computed from $-\rho_0 g\zeta$ with tidal heights ζ taken from the M_2 solution of FES2012. The global density grid used for both figures is a 2001–2010 mean from ERA-Interim 1° data referred to the orography instead of mean sea level.

that would be registered by a barometer that is moving vertically with the body tide in an otherwise unperturbed atmosphere (characterized by air density ρ_0 and gravity acceleration g). Under real atmospheric conditions, equation (2) is a correction term to the pressure tide L_2, which, at the Earth's surface, lags less than 15° relative to the local mean lunar time [*Chapman and Lindzen*, 1970]. Owing to this phase constellation, the body tide contribution to L_2 for crust-fixed barometers is thus a distinct amplitude reduction with respect to the pressure variations at a fixed geopotential surface [*Miyahara*, 1972].

The signal component in equation (2) is further modulated by a small contribution from ocean tidal loading, which in terms of observed pressure ($-\rho_0 g\zeta$) rarely exceeds 2 μbar over land but causes regional seafloor deformations of up to 6 μbar. We have deduced a global 1/16° chart of this secondary perturbation by mapping elevations from a state-of-the-art ocean tide model, Finite Element Solution 2012 (FES2012) [*Carrère et al.*, 2012], to vertical displacements based on the Green's function approach of *Dill and Dobslaw* [2013]. The superimposed signal of body and ocean load tide effects on surface pressure is shown in Figure 1a. It can be interpreted as the barometric lunar tide due to the mere up and down motion of the Earth's surface, and it is

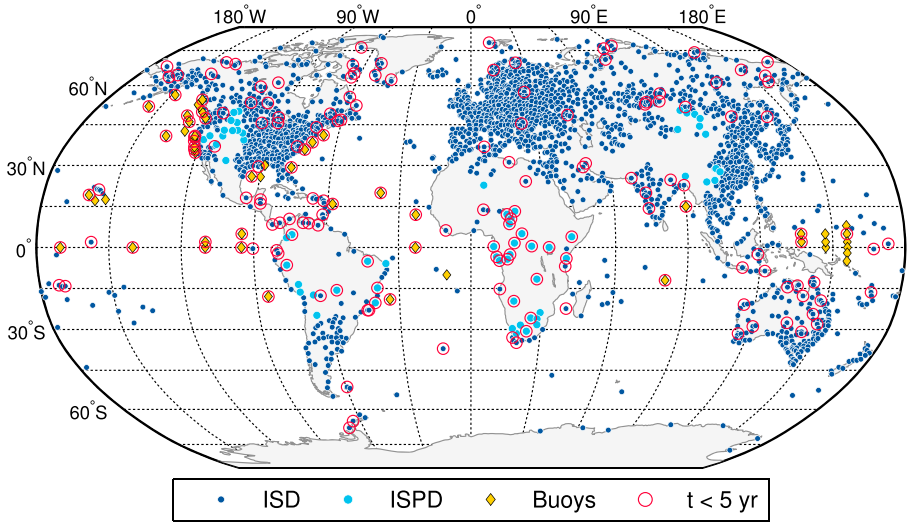

Figure 2. Geographical distribution of the 2315 L_2 estimates as determined at 2198 ISD land stations (dark blue circles), 64 ISPD land stations (light blue circles), and 53 buoy platforms (yellow diamonds). Locations with barometer time series shorter than 5 years are additionally brought out by red circles. The median time series length is 18 years.

implicitly contained in available lunar tidal models [*Haurwitz and Cowley*, 1969; *Goulter*, 2005] that have been inferred exclusively from barometric data recorded at land or island stations.

In the present work, we also use tidal estimates from floating buoys and therefore extend our considerations to the moving boundary between the atmosphere and the oceans. In fact, sensors attached to the sea surface will observe a lunar tide that is composed of (i) the actual air tide relative to a reference surface at rest, (ii) a signal due to the lifting of the water column in the wake of body + load tide, and (iii) another lifting term, δp_{M_2}, induced by the oceanic M_2 tide. Figure 1b provides a global chart of δp_{M_2} computed on the basis of the nominal pressure lapse rate $(-\rho_0 g\zeta)$ and the FES2012 tidal heights ζ as introduced above. Evidently, in regions of strong M_2 elevation changes, pressure sensors aboard ships or buoys register large barometric tidal signals (up to 150 μbar) that are distinctly different from the manifestations of the L_2 tide at nearby continental sites. Yet both groups of sensors require a common vertical datum to allow for a feasible spatial interpolation of the signal in a global domain and also across the coasts. We therefore subtract from all marine registrations the ocean tidal lifting effect δp_{M_2}, which will be referred to as the "static contribution of M_2 to the atmospheric tide." The remaining dynamic component of L_2, discussed in the following, is thereby fully consistent with the analysis of *Haurwitz and Cowley* [1969] in terms of the underlying reference surface. It should, however, be kept in mind that for geodetic applications as well as studies of the energy balance in the lunar air tide [*Platzman*, 1991], both dynamic and static components need to be considered.

3. New L_2 Ground Truth Data

Our network of lunar tidal harmonics consists of 2315 estimates at land stations and buoys, distributed across the globe as shown in Figure 2. The large portion (2198 stations) of this compilation has been computed from hourly to 3-hourly synoptic observations of the ISD for an analysis window from 1900 to 2010 to maximize the positive impact of time series length on the accuracy of lunar tidal determinations. The quality-controlled ISD archive arguably provides a sea level pressure (SLP) subset of the closely related International Surface Pressure Databank (ISPD) [*Cram et al.*, 2015], which has been mapped to empirical models of the solar S_1 and S_2 tides by *Schindelegger and Ray* [2014] but proved to be technically less suited for our century-long analysis attempt. A small number of continental fill-ins (64 stations), mostly located on the African continent, are based on ISPD data, though, and the geographical coverage has been further improved by incorporating estimates from 53 stationary marine platforms, comprising ISPD buoys in higher latitudes and 24 equatorial sensors from the Tropical Moored Buoy Array [*McPhaden et al.*, 2010]. Note, however, that the time series length of many of these additions is only a few years (cf. Figure 2), leading to greater uncertainties in the associated tidal estimates. While special attention has been devoted to such critical cases, our analysis strategy is mostly automated. We discuss its main features below.

3.1. Time Series Preparation and Tidal Analysis

Notwithstanding the variety of L_2-specific estimation methods [*Chapman and Lindzen*, 1970; *Kohyama and Wallace*, 2014], a standard least squares fit of harmonic constants appears to be the most appropriate technique to estimate the lunar tidal signal for several thousands of barometer time series with heterogeneous sampling characteristics. Such an approach requires, however, the reduction of lower frequency meteorological pressure variations through filtering, preferably on the basis of equidistant temporal coverage. To that end, each barometer series was screened for breaks <7 days, separated into the resultant portions, and subject to spline interpolation to eight synoptic hours (usually 0000, 0300, 0600 UTC, etc.) within each of these blocks. With small inner data gaps of 12 h allowed for, only a fractional, if any, part of the local pressure series had to be interpolated, and our final L_2 estimates are thus barely sensitive to the details of the interpolation method. The actual filtering of each time series block was accomplished by a third-order Butterworth high pass with a cutoff frequency of 0.4 cycles per day.

The multiyear filter residuals were then tidally analyzed over the whole time period and for the three customary "Lloyd" seasons, defined from May to August (June solstitial or J season), November to February (December solstitial, D), and the equinoctial (E) months of March, April, September, and October [*Haurwitz and Cowley*, 1969]. Accordingly, only one third of the time series, comprising the relevant months, is eligible for the estimation of seasonal L_2 splits. We imposed a condition of approximate equipartition of observations between the different seasons, whereby barometer series with either J, D, or E observation counts deviating more than 10% from the corresponding $\overline{\mathrm{JDE}}$ mean count were dropped from further consideration.

Contrary to the usual practice in air tide studies, we refer our phases ϕ to the M_2 equilibrium tidal peak V at the Greenwich meridian as commonly employed in oceanography [*Pugh and Woodworth*, 2014] and adjust the basis sinusoids for small time-dependent nodal variations in amplitude and phase, labeled as f and u. Our functional model of L_2 at any location thus reads

$$\mathrm{L}_2(t) = Af\cos(\omega t - \phi + (V+u)), \tag{3}$$

complemented by customary S_1 and S_2 harmonics with phases referred to 0 UTC. In equation (3), A denotes the tidal amplitude, $\omega = 1.405189 \cdot 10^{-4}$ rad s^{-1}, and t is time in seconds relative to a reference epoch for which the equilibrium phase V has been computed. Standard errors of the tidal constants, although not thoroughly discussed in the remainder of this work, were derived in the fashion of *Ray* [1998] based on repeated tidal analysis in ℓ disjoint yearly segments. Amplitude errors σ_A may be then computed from the sample standard deviation of ℓ realizations of A, scaled by $t/\sqrt{\ell}$, where t is the 0.95 quantile of a two-tailed Student distribution with ℓ degrees of freedom. Phase errors were approximated by the ratio of σ_A/A in radians.

3.2. Selection Criteria

Subsetting the 110 year history of ISD pressure data to a global barometer compilation for tidal studies is the most delicate task of this work. While having been quality controlled prior to publication [*Lott*, 2004], the ISD may well entail a hodgepodge of good and bad tidal data, which need to be distinguished in the best possible way through automated means. We build on algorithms developed by *Schindelegger and Ray* [2014] for a related analysis of S_1 and S_2.

The ISD station inventory of over 29,300 entries was first limited to about 19,900 nonmarine sites that provide complete positional information and observational coverage of at least 3 years. The time series of these candidates were subsequently screened for suitable runs of barometric data in the sense that an integral number of calendar years (≥3)—occasionally interrupted by gaps of no more than 7 days—had to display subdaily, i.e., mostly 3-hourly, sampling as evident from the total number of observations and the composition of the daily mean pressure cycle. Guided by the S_1/S_2 analysis of *Schindelegger and Ray* [2014], we identified epochs of the mean day composite that were sampled at least 600 times and required their distribution within [0000; 2400] UTC to be distinctly uniform and to comprise seven or more samples. By retaining only these core epochs in the probed time series, we mitigated the impact of irregular subdaily registrations that are often indicative of malfunctioning pressure sensors or time-stamping issues.

ISD exclusively provides SLP data instead of the pressure values observed at altitude. This custom necessitates an additional station restriction in terms of elevation, since vertically reduced pressure measurements are susceptible to distortions of the tides in the wake of dubious temperature-averaging techniques [*Mass et al.*, 1991]. *Covey et al.* [2011] showed that a <1 km constraint on SLP sites removes essentially all aliasing problems for the solar S_2 harmonic, and one of our initial global L_2 scatters indicated that this limitation

is indeed required to eliminate inconsistencies of lunar tidal determinations across regions of considerable height variations, e.g., North America or Southeast Asia. Specifically, SLP-based L_2 amplitudes over the Tibetan Plateau/western China are significantly (~20%) higher when compared to their surface pressure pendants provided by the ISPD. We used the latter data set to fill up some of the gaps arising from the 1 km constraint on SLP sensors, but only moderately so, as the ERA-Interim tide is validated at mean sea level, and inertia-gravity wave propagation characteristics both in the vertical and in the vicinity of high topography likely cause tidal amplitude changes [*Hamilton et al.*, 2008].

Applying the selection, filtering, and harmonic analysis techniques devised above, a first, plausible guess of L_2 tidal constants at over 7700 ISD sites could be obtained. This compilation was understandably glutted with estimates of mixed reliability throughout Europe, the U.S., East Asia, and parts of Australia, thereby requiring further cleaning and subsetting. We adopted a self-iterative approach for this purpose without using any external information. First, globally gridded L_2 priors for annual and seasonal terms were deduced through multiquadric (MQ) interpolation of the longest pressure time series in regular 1.5° cells. Values for the multiquadric and smoothing parameters were taken from the S_2 solution of *Schindelegger and Ray* [2014], allowing for a slightly increased smoothing of the seasonal splits given the larger scatter in those estimates. We then analyzed site-wise RMS (root-mean-square) statistics of station tide versus MQ harmonics for annual and seasonal bands and singled out suspicious stations where RMS values in one of these bands appeared to be significantly higher than the mean RMS difference of all neighboring sites. In particular, a weighted average based on time series length was constructed from data points within 20° spherical distance, and in case the test RMS exceeded this reference value by more than 50% (70% for J, D, and E), the examined station was flagged for iteration. We employed a simple outlier-trimming using 3 sigma limits for this second stage of time series preparation in order to eliminate remaining gross observational spikes or to reduce subdaily pressure perturbations associated with storm events [*Ray*, 2001]. Tidal estimates from these edited station data were once more assessed for their RMS differences with respect to the MQ priors and ingested to the compilation if the statistics warranted to do so. Approximately 500 of the 3450 initially rejected stations could be recovered in this manner.

Our refinement algorithms were applied not only to all continental areas north of 30°N but also to numerous regional boxes with dense station coverage at the U.S. Gulf Coast, Argentina, Saudi Arabia, India, Southeast Asia, Australia, and New Zealand. All other regions of the Earth, including Africa, Latin America, and most of the oceanic islands are sparsely covered by meteorological sensors but pivotal to the representation of the global L_2 tide. It is therefore appropriate to analyze their barometer series with more rigor, i.e., by using the same processing strategies as described above but allowing for intermediate visual assessments of (i) the filtered time series, (ii) the distribution of seasonal terms in relation to the annual mean, and (iii) the consistency with tidal harmonics from neighboring stations. There is an admittedly fine line in deciding whether estimates from more isolated sites and short barometer records can be deemed reliable despite the availability of L_2 a priori knowledge from *Haurwitz and Cowley* [1969] or *Vial and Forbes* [1994]. In general, our approach was to maintain even somewhat debatable harmonics from remote sites and rely on the eventual MQ gridding to smooth out any larger inconsistencies.

From the vast initial ISD collection, a total of 4154 SLP stations was retained and subsequently augmented by estimates from 64 ISPD land locations and 53 marine platforms. In detail, the ISPD stations are surface pressure sensors at higher altitudes (but still <2 km) over the western U.S. and East Asia, separated by at least 0.5° from the nearest data point. Somewhat relaxed time series constraints (e.g., only 2 years of data) had to be adopted to capture individual Central African ISPD locations as well as most of the tropical moored buoys, which provide excellent hourly barometric records, though. Consistent with our argumentation in section 2, all pressure time series from marine platforms were corrected for their vertical motion associated with the oceanic M_2 tide prior to the harmonic analysis. We obtained the necessary elevation information, adjusted for variations of the lunar node, from the Tidal Model Driver of *Padman and Erofeeva* [2005], taking an altimetry-based inverse model (TPXO7.1, updated version of *Egbert and Erofeeva* [2002]) as the basis data set. Air density values were interpolated to the buoy locations from a 1° climatological mean field of ERA-Interim during 2001–2010.

An obscure timekeeping error of 100 min, borne out by observation epochs at 0140, 0440, 0740 UTC, etc. and a bias of the S_2 phase with respect to a reference model [*Ray*, 2001], occurred for 11 stations in Chad, Gabon, Congo, and the Central African Republic. The very same stations are undetected S_2 contaminations in

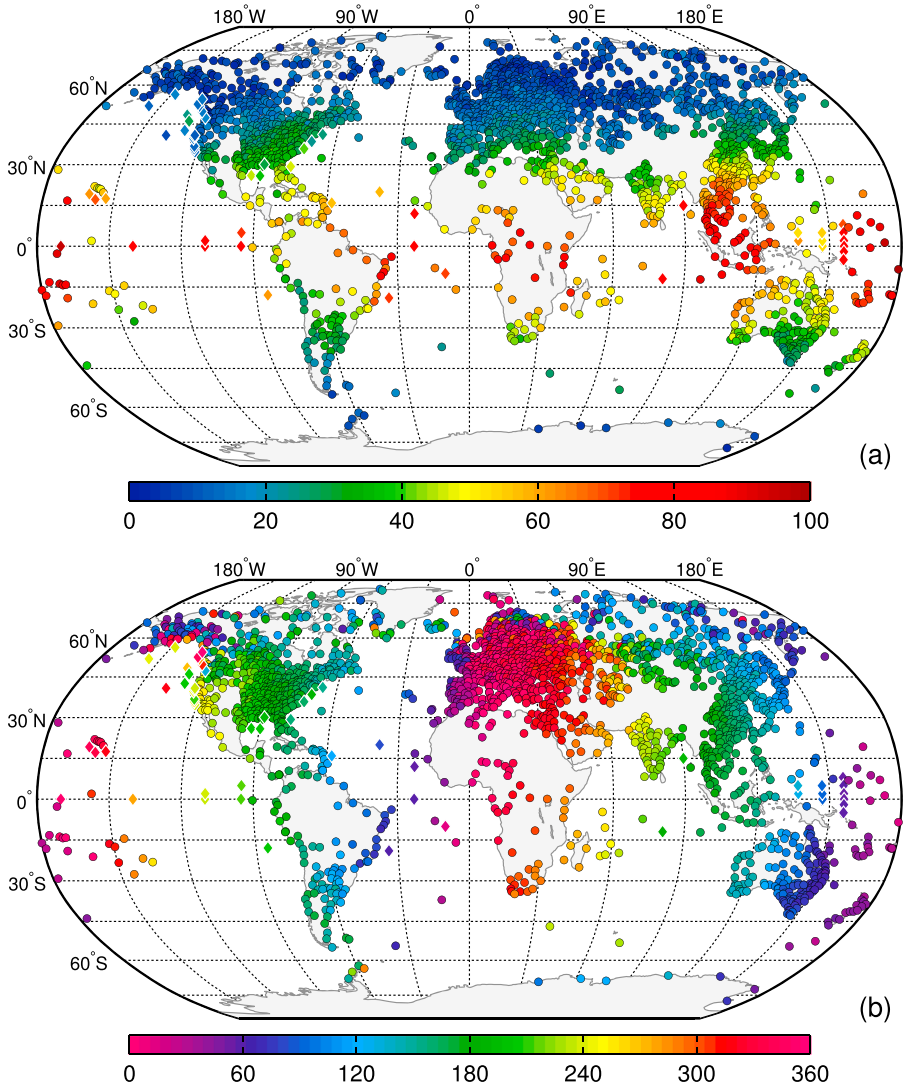

Figure 3. (a) Annual mean amplitude in μbar and (b) phase of the lunar air pressure tide L_2 for 2315 ground truth stations, with buoy locations shown as diamond markers. Phase lags in degrees are reckoned relative to the tidal argument of the M_2 equilibrium tide at Greenwich.

Figure 5b of *Schindelegger and Ray* [2014] but have been corrected in the present analysis. Our final collection of 2315 tidal determinations was derived through conserving in each 1.5° cell only data from the longest observing land barometer and merging this high-quality subset with the 53 buoy platforms.

3.3. Discussion of L_2 Estimates

Amplitude and Greenwich phase lag plots of the new L_2 compilation are shown in Figure 3 for the annual mean. Both the internal consistency of the estimates and their spatial distribution are clearly sufficient to quantify the major characteristics of the semidiurnal lunar pressure tide even from raw scatterplots. A wavenumber 2 pattern of slight north-south asymmetry and with equatorial peak amplitudes of about 100 μbar uniformly propagates westward, lagging the tide-raising body by about 15° – 30°; cf., e.g., the phase values at the 0° and 180° meridians. Zonal interruptions in amplitude, which are far less pronounced in *Haurwitz and Cowley*'s [1969] gridded solution given the gaps in their ground truth data, are evident at least in the proximity of $\lambda = 150°$W (Central Pacific), 75°W (Andes), and 140°E (New Guinea).

A particularly seamless representation of L_2 is achieved for data clusters in the northern latitudes, Southeast Asia, and Australia, where consistency between neighboring estimates was enforced through our iterative selection technique and the emphasis on long barometer records. Maximum durations (69 years) are found

at Annette Island Airport, Alaska, and Honolulu International Airport, Hawaii, and time series lengths of more than three decades prevail over Europe, East Asia, and most of the U.S. Amplitude errors σ_A in these regions are 5 μbar when mapped to a median value and do not exceed 10 μbar for 90% of the involved stations. Associated phase errors scale inversely with amplitude (section 3.1) but are generally below 25° away from Arctic and sub-Arctic latitudes. Other more sparsely sampled regions of the globe feature mixed station tide statistics, ranging from $\sigma_A \sim 5-10$ μbar at most islands and buoys to more than 20 μbar in Central Africa and the South American Tropics (Columbia, Venezuela); cf. the locations of very short barometer time series (2–4 years) in Figure 2. Nonetheless, the harmonics from these suspect data points blend in well with the surrounding estimates from longer records.

Space precludes a detailed assessment of our station tide data for individual seasons, and we refer the reader to the electronic supplement for J, D, and E season scatterplots analogous to Figure 3. In terms of its general characteristics—e.g., amplitude maxima occurring during the J months, as well as later lunar peak times and somewhat stronger hemispheric asymmetries for the D months—the seasonal variability of the present L_2 solution conforms well with the results of *Haurwitz and Cowley* [1969]. At this place, we only quantify how the internal consistency of our compilation varies across the deduced partitions. Following *Ray* [2001], we identified station pairs within 200 km distance of each other for latitudes lower than 50° degrees and computed the RMS difference of their respective L_2 estimates. Averaged over 1873 retrieved station pairs, the mean RMS for the annual scale is 4 μbar and thus only about 10% of the mean lunar tidal amplitude $\bar{A} = 37$ μbar in a $|\varphi| \leq 50°$ subset. The seasonal partitions yield higher dispersion statistics at roughly 6–7 μbar, which constitutes almost 20% of the mean amplitudes for D ($\bar{A} = 33$ μbar) and E ($\bar{A} = 37$ μbar) terms. This is undoubtedly an indication of the larger statistical uncertainty of tidal determinations if they are based on limited observational data.

In what follows, we use our empirical knowledge of the barometric lunar tide to validate the output of reanalysis models. To that end, a globally gridded representation of L_2 on both the annual and seasonal scales was computed by aid of an objective interpolation with the MQ technique as outlined by *Nuss and Titley* [1994]. We adopted a 2° × 2° latitude-longitude grid and phrased *Nuss and Titley*'s [1994] equations for spherical problems. The shape parameter of the radial basis functions as well as the amount of smoothing were those of the S_2 interpolation in *Schindelegger and Ray* [2014], due to the mere fact that this tide resembles L_2 in its spatial appearance and is also dominated by a migrating wavenumber 2 component.

4. Validation of L_2 in Global Reanalyses

Reanalyses are systematic approaches to climate and weather research in which a long-term record of the state of the atmosphere is developed from the objective combination of observational data and a global numerical model. Specifically, the prescribed physics, the numerical scheme, and the data assimilation components are held constant and exposed to a time-varying network of observations. In ERA-Interim, both conventional surface and upper air data as well as remotely sensed observations have been assimilated for the satellite era from 1979 up to the present times. A stepping stone toward a more comprehensive reanalysis has been recently made available in the form of ERA-20C, the ECMWF pilot reanalysis of the twentieth century based on surface observations only [*Poli et al.*, 2013]. Rather than serving research requirements, ERA-20C has been designed to assess the performance of new data assimilation methods that efficiently deal with the changing observing system during the twentieth century. Input data are surface pressure reports from ISPD and the International Comprehensive Ocean-Atmosphere Data Set (ICOADS) [*Woodruff et al.*, 2011] as well as ICOADS wind vectors above the surface of the oceans. Given this limitation, ERA-20C is of lower rank compared to other available reanalyses but it functions as a welcome test bed to study the linkage between L_2 and in situ observations in global assimilation models.

For both reanalyses, four times daily global sea level pressure data on a 2.5° latitude-longitude grid were extracted from the respective ECMWF archives. Record lengths are 1979–2010 (ERA-Interim) and 1900–2010 (ERA-20C), even though only the post-1978 data of the latter model are utilized in this section. Pressure time series at each location were high-pass filtered (0.4 cycles per day cutoff) and cleared of the dominant S_1/S_2 lines by repeated subtraction of a daily composite cycle built from the pressure averages at 0000, 0600, 1200, and 1800 UTC. Tidal constants of L_2 were then retrieved from a standard least squares fit in the manner of section 3.1. We repeated the very same analysis for the J, D, and E seasons after curtailing the initial time series to the relevant months.

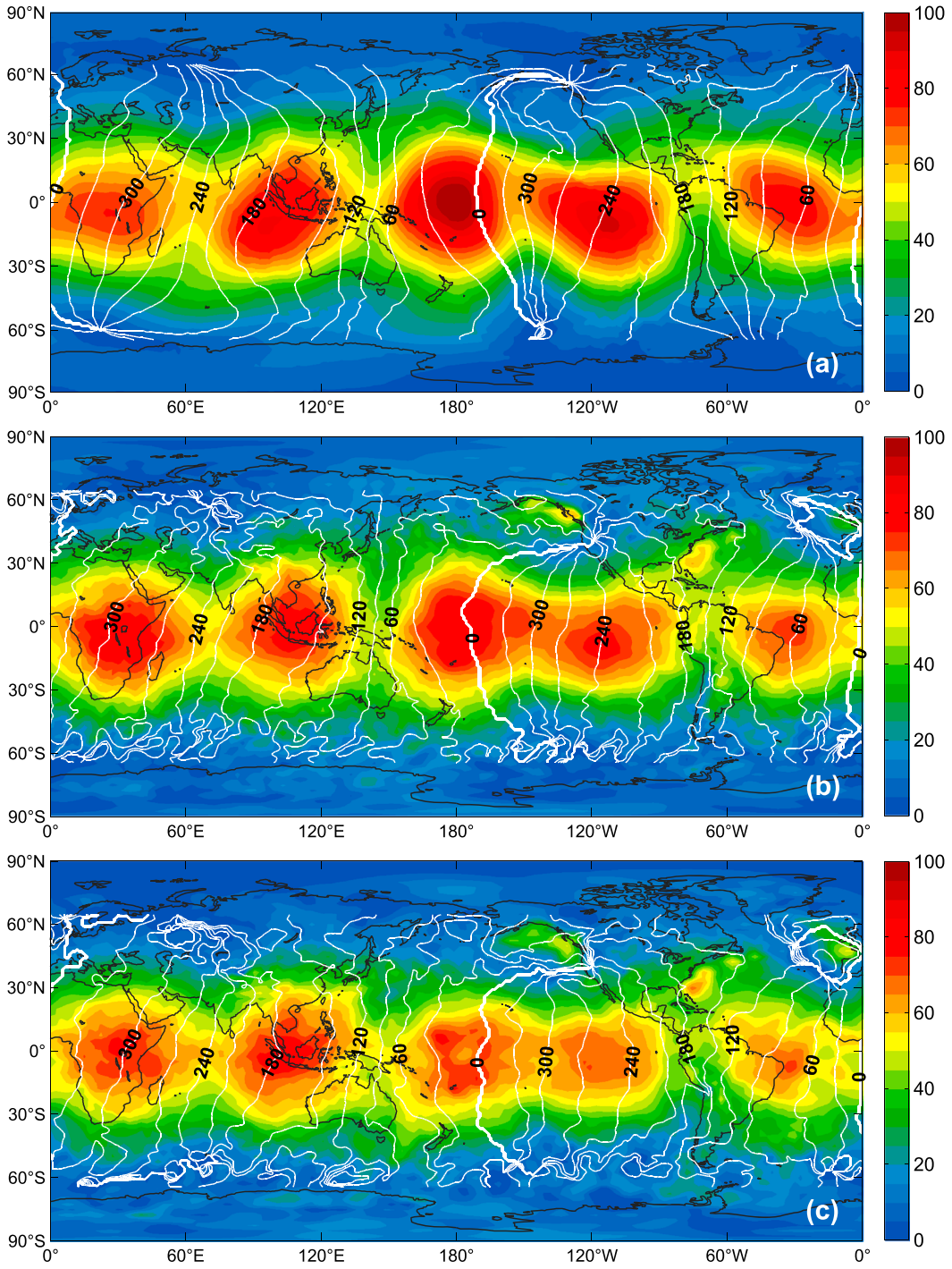

Figure 4. Cotidal charts of the annual mean barometric L_2 tide for (a) our gridded empirical model based on ISD in situ data, (b) ERA-Interim sea level pressure during 1979–2010, and (c) ERA-20C sea level pressure also averaged through 1979–2010. Color-filled contours show amplitudes in μbar, and white isolines indicate Greenwich phase lag every 30°, a lag of 0° being shown by the bold line. Note that the central meridian is at 180° compared to Figure 3.

Table 1. Comparison Between Station Tide Estimates and the Interpolated L_2 Tidal Constants for ERA-Interim, ERA-20C, and the MQ-Gridded Empirical Model[a]

	Annual		J Season		D Season		E Season	
Model	RMS	$\Delta\phi$	RMS	$\Delta\phi$	RMS	$\Delta\phi$	RMS	$\Delta\phi$
ERA-Interim	5.7	−4.2°	7.3	−3.7°	8.3	−2.9°	8.0	−4.5°
ERA-20C	5.1	1.6°	7.1	1.9°	7.7	2.3°	7.6	0.5°
MQ	3.2	0.2°	4.9	−0.1°	5.5	1.1°	5.2	−0.5°
Signal[b]	23.8		28.1		22.3		24.2	

[a]Statistics are globally averaged RMS differences (μbar) and median differences in Greenwich phase lags, $\Delta\phi$ (deg), reckoned in the sense model minus station. If estimates from buoys are excluded from the statistical analysis, all RMS differences would decrease by 0.2 μbar.

[b]Signal values were computed from $\sqrt{\overline{A_s^2}/2}$, where A_s are pressure tide amplitudes at the respective stations, and the overbar denotes global averaging.

Figure 4 displays annual mean L_2 charts for our gridded empirical model, ERA-Interim, and ERA-20C. A remarkably close agreement between reanalysis tides and the in situ solution is readily apparent, even though that similarity might have not been expected per se. Specifically, we have imposed the moving crust as a reference datum for our tidal estimates, whereas global analysis models prescribe an invariant Earth surface and also discount vertical sensor displacements over the oceans. Yet these inconsistencies have a surprisingly small impact on the lunar tidal signal in the ECMWF models; the appearance of L_2 resembles closest to the tide that is referred to the oscillating crust, presumably due to the abundance of continental barometers in the assimilation process.

The global L_2 signal that develops from the combination of model physics and observations in the reanalyses deviates from the ground truth tide (Figure 4a) in a few aspects. Rather smooth spatial characteristics of L_2 in the MQ solution contrast to considerable jitters in the numerical models and can be attributed in parts to the repeated usage of smoothing in deriving our empirical tidal model (sections 3.2 and 3.3). The small-scale fluctuations of the tide seen in reanalyses are, however, not necessarily physical and may be well artifacts from the imperfect spatiotemporal distribution of meteorological input data. Moreover, ERA-Interim as well as ERA-20C tend to underestimate L_2 in the Tropics, particularly over oceanic areas with comparatively little maritime traffic such as the equatorial Pacific [see *Poli et al.*, 2013, Figure 3]. Peak amplitudes around the 180° and 120°W meridians are 70–80 μbar and therefore more than 20 μbar smaller than our empirical estimates, even though a restriction to the last decade in ERA-Interim (2000–2010) reduces this discrepancy to only 10 μbar (not shown). We emphasize that the East Pacific in situ maximum of 100 μbar is well constrained by an adequate network of stations and buoys (Figure 3), and a similar regional enhancement of the tide at 180° exists in the L_2 simulations of *Vial and Forbes* [1994] (120 μbar for July, with the annual mean amplitude being roughly 20 μbar smaller).

Other more local deficiencies of the ERA tidal solutions are evident off the coast of Alaska, the eastern U.S., and Great Britain. These patterns coincide with maxima in the M_2 ocean tide (Figure 1b) and have been densely sampled by barometers aboard marine objects over the full reanalysis period. They thus enter the assimilation system as realizations of the static ocean tide contribution to L_2—a fact that is also borne out by the correspondence of phase values of δp_{M_2} in Figure 1b and L_2 in Figures 4b and 4c across the Gulf of Alaska and near the British Isles. These local signals are, however, inconsistent with global wave dynamics as well as the assumption of an invariant reference surface. They are therefore suppressed by the analysis procedure, in particular at locations where δp_{M_2} is effectively out of phase with the uniform westward propagation of the dynamic L_2 tide. Based on these anomalies, *Kohyama and Wallace* [2014] have suggested that also the zonally varying structures of L_2 in the Tropics are repercussions of the ocean tidal lifting effect. Our results (Figure 4a) question that view; the separation into five regional maxima is a distinct characteristic of the crust-referred tide, and even for reanalyses the impact of δp_{M_2} from vertically displaced marine sensor data appears to be minimal in latitudes below 30°.

Additional subtle differences among the probed L_2 models are disclosed by the statistical comparison provided in Table 1. Considering all 2315 in situ locations, we have computed globally averaged RMS misfits and median phase lag differences $\Delta\phi$ between station and reanalysis tides for the annual mean and the three

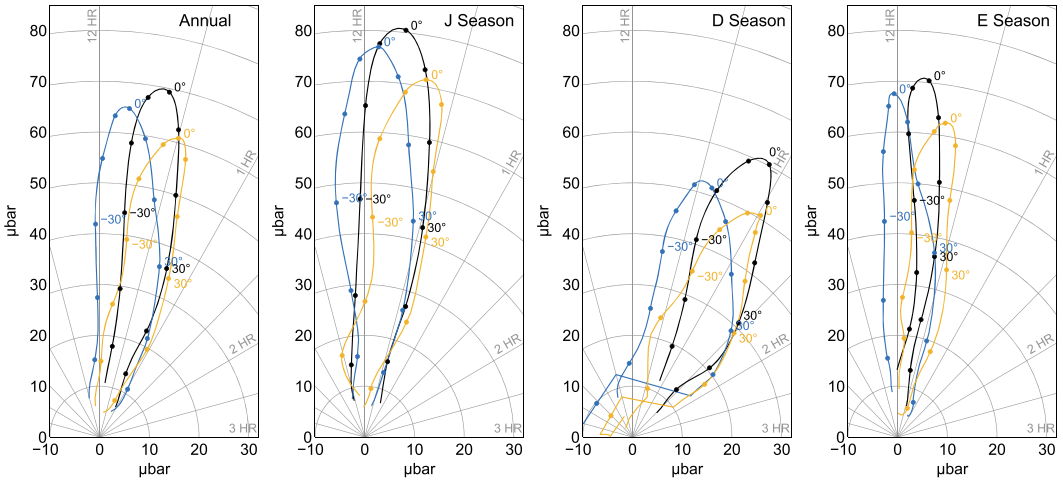

Figure 5. The wavenumber 2 component of the barometric L_2 tide as a function of latitude plotted on a harmonic dial with times of maximum pressure reckoned clockwise in lunar hours from the Moon's passage through the meridian. Results are displayed in terms of annual mean and the three Lloyd seasons for the climatologies derived in this paper (black curves), ERA-Interim (blue curves), and ERA-20C (orange curves). Dots indicate the computed values every 10th degree of latitude up to $|\varphi| = 60°$. All curves were moderately smoothed by a five-point running average filter.

conventional seasons. This comparison is not completely rigorous, since considerable portions of the analyzed pressure data as from 1979 are also assimilated in ERA-Interim and ERA-20C. Yet a spin-off of our ISD analysis based solely on pressure records prior to 1979 yielded results very similar to the ones presented below.

Tabulated RMS misfits of both ECMWF solutions with ground truth data are below 6 μbar on the annual scale but increase to 7.1–8.3 μbar for the seasonal splits, owing to the larger stochastic variability in station and reanalysis determinations of L_2 when only three months per year are considered. Interestingly, ERA-20C produces lower RMS differences than ERA-Interim for the annual and all seasonal terms. The corresponding variance reduction is significant at the 0.01 level (excepting the J season), probably as a reflection of the increased weight of surface pressure data in the ERA-20C assimilation procedure. Median phase differences with ground truth estimates are also marginally better for ERA-20C (around 2° in the sense model minus station) than for ERA-Interim (−4°). Such small values of $\Delta\phi$ contrast strongly with what is usually obtained from in situ validations at the solar semidiurnal frequency [*Schindelegger and Ray*, 2014] where model artifacts from the coarse time stepping of radiation processes must be accepted [*Poli et al.*, 2013]. Table 1 also includes RMS and phase lag statistics for our empirical L_2 solution to emphasize the suitability of the adopted MQ gridding technique. RMS misfits with the original tidal estimates vary from 3.2 μbar (annual mean) to 5.4 μbar (D season) and are partial measures of the station-to-station irregularities that have been mitigated by smoothing.

We complement this section with harmonic dial representations of the various L_2 climatologies in terms of their wavenumber $s=2$ component, abbreviated as L_2^2. This is the main wave of the lunar atmospheric tide, traveling westward with the Moon around the Earth. It is readily extracted from a Fourier decomposition of the complex-valued $Ae^{i\phi}$ grid (equation (3)) to a two-sided spectrum of wavenumbers s versus latitude; cf. also *Covey et al.* [2011] and the harmonic analysis method of *Haurwitz and Cowley* [1969]. After curtailing the spectrum to $s=2$, we deduced latitudinal profiles of amplitude and phase (ϕ) variations. The conversion of phase lags on the equilibrium tide to local lunar time of maximum pressure T_{max} (in lunar hours) reads [*Kohyama and Wallace*, 2014]

$$T_{max} = \frac{24 \text{ lunar hours}}{4\pi} (\phi + 2\lambda) . \tag{4}$$

Figure 5 depicts the distribution of the main migrating mode for the annual mean and the three Lloyd seasons. Consistent with what has been found by *Haurwitz and Cowley* [1969], hemispheric asymmetries are least pronounced in the E season but well developed during the D season with a particularly late appearance of peak pressures in northern latitudes (1–2 lunar hours). Given the paucity of stations in the compilation of *Haurwitz and Cowley* [1969], migrating amplitudes at the equator are persistently higher in our ground truth model, by about 6–9 μbar, and a systematic shift to earlier peak times (−15 min in T_{max}) is seen in all seasons.

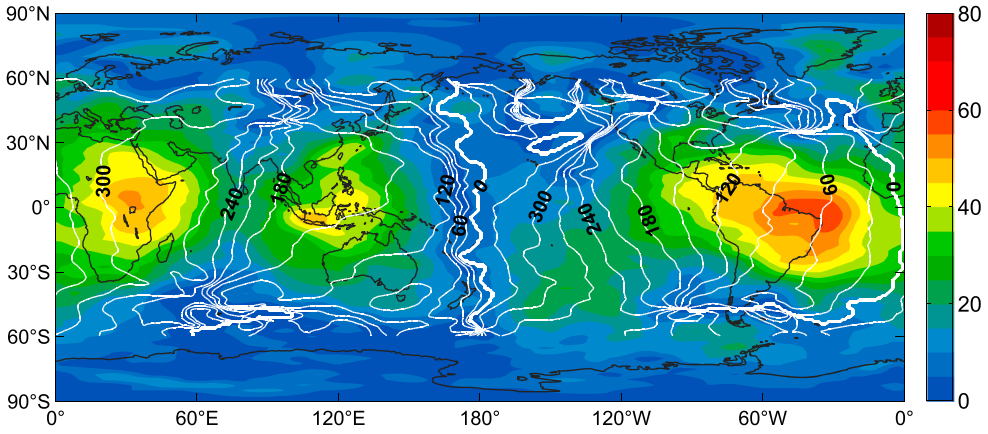

Figure 6. Cotidal map of the annual mean barometric L_2 tide in ERA-20C sea level pressure data during 1900–1930. Color-filled contours show amplitudes in μbar, and white isolines indicate Greenwich phase lag every 30°. Wavenumbers greater than 15 have been removed from the representation. Note the amplitude cap at 80 μbar compared to Figure 4.

The wavenumber 2 terms of ERA-Interim and ERA-20C show little deviation from the in situ-based profile in northern latitudes down to 30°N, likely due to the plethora of barometric data in the assimilation. South of 30°N, the L_2^2 distribution is somewhat more divergent; ERA-20C yields correct phases but underestimates the pressure tide by about 10 μbar. By contrast, ERA-Interim produces slightly deficient peak times that lead the empirical reference values by 10–15 min. This is probably a significant correction to Figure 3 of *Kohyama and Wallace* [2014], which suggests that the lunar air tide at the Earth's surface lags the Moon's transit by only 7 min. We repeated their computation of a mean, area-weighted L_2 phase lag within 30°N–30°S using the ERA-Interim and MQ-gridded Greenwich phases ϕ depicted in Figure 4. The corresponding value of T_{max} is 13 min for the reanalysis tide as opposed to 24 min in our in situ solution. Note also that the tidal estimator of *Kohyama and Wallace* [2014], based on a differentiation of regression maps at four epochs of a mean solar day, can entail small spurious phase increments of 5–10 min with respect to our rigorous implementation using lunar time and equilibrium phases (T. Kohyama, personal communication, 2015).

Other components of our zonal wavenumber decomposition were briefly examined, leading to a somewhat different picture of nonmigrating modes compared to *Haurwitz and Cowley* [1969], whose results for minor waves have been questioned by *Vial and Forbes* [1994] and also by *Goulter* [2005]. In particular, the distinctive five-peak structures of our empirical L_2 tide can be reconstructed with reasonable accuracy from a mere superposition of the $s=2$ main mode and an eastward propagating $s=-3$ component that attains amplitudes of 13 μbar at the 10°S parallel. Even though the exact forcing mechanisms of this $s=-3$ feature in the air tide are preferably identified through numerical modeling, we emphasize that a nonmigrating $s=-3$ mode of very similar amplitude (17 μbar along 30°S in terms of air pressure, $\rho_0 g\zeta$) is also found in the wavenumber spectrum of the M_2 ocean tide.

5. Dependency of the Model Tide on Observations

The previous section has unveiled a credible barometric lunar tide signal in the ERA-20C reanalysis that draws all of its observational constraints from conventional meteorological registrations of surface pressure and marine winds. This fact is in itself a testament to the relevance of in situ data in accounting for the realistic L_2 oscillation in the analysis systems of the ECMWF. An examination of ERA-20CM, a data-free sibling of ERA-20C driven only by solar, marine, and volcanic forcing [*Hersbach et al.*, 2015], underpins that view. We have analyzed this model-only integration for the atmospheric tidal variability in the manner of section 4 but found no evidence of any deterministic signal. Therefore, the lunar tide in ERA-20C must originate from the observations; cf. an analogous conjecture by *Kohyama and Wallace* [2014] based on ERA-Interim. In what follows, we work out the dependency of the L_2 model tide on the evolving observing system of the ERA-20C experiment.

Figure S5 in the supporting information depicts a series of L_2 determinations in 20 year windows commencing 1900. This is a backward extension to our nominal 1979–2010 window and illustrates how the barometric tide in ERA-20C grows and gradually develops the fidelity seen in Figure 4c. The reader is encouraged to juxtapose these plots to the coverage maps of station and ship observations given in *Poli et al.* [2013] or at

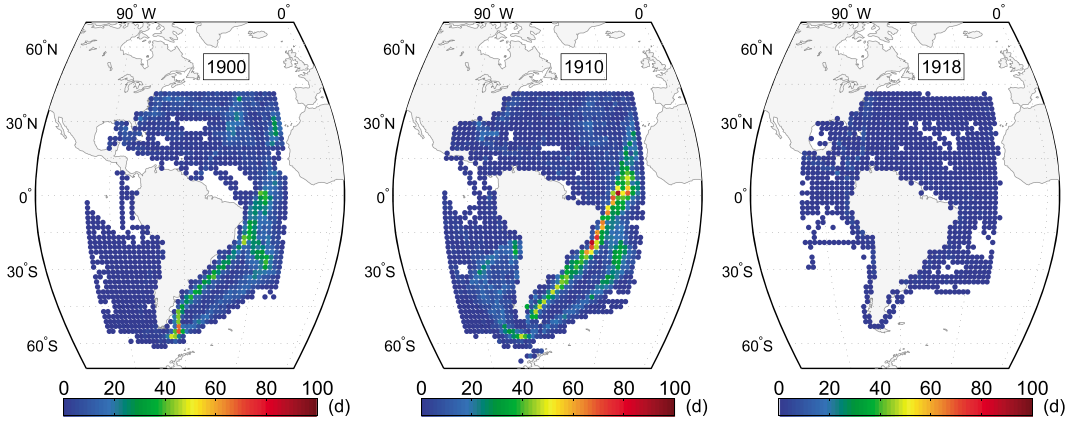

Figure 7. Illustration of the ICOADS data frequency for the years 1900, 1910, and 1918 within a regional box bounded by 40°N–70°S/100°W–20°W. In each year, the ICOADS pressure observations were binned to 2° cells, and the number of days holding high-frequency observations (6-hourly samples at least three times per day) was accumulated cell wise.

http://icoads.noaa.gov/r2.5slp.html (accessed September 2015, reprinted in our electronic supplement) for the ICOADS Release 2.5. Here we provide an additional chart of the lunar air pressure tide for the averaging period 1900–1930 in Figure 6. The L_2 characteristics of this representation are rudimentary but comprise a largely uniform westward phase increase as well as persistent amplitude maxima of about 35–50 μbar across the equatorial Atlantic and adjacent landmasses. The obvious similarities of these oscillations with the eventual pressure tide in ERA-20C are somewhat surprising given that only a few isolated station barometers are available for assimilation in the Tropics during the first decades of the twentieth century; cf. the yearly ISPD networks cataloged at http://www.esrl.noaa.gov/psd/cgi-bin/data/ISPD/stationplot.v2.pl (September 2015). In contrast, ship-recorded pressure and surface wind measurements constitute a much more extensive pool of input data around 1900, and we thus suppose that marine observations stir up the initial L_2 signal in ERA-20C.

This assumption requires, of course, some substantiation. A pertinent data frequency assessment was performed based on ICOADS samples within a regional box centered around South America (40°N–70°S and 100°W–20°W, respectively). Corresponding pressure observations during 1900–1930 were downloaded from archives at the NCAR (National Center for Atmospheric Research) Data Support Section and binned to 2°×2° boxes for each calendar year. To induce and maintain in the ERA-20C assimilation system a large-scale L_2 wave that does not leak into the nearby S_2 band, a certain amount of these ocean boxes must feature subdaily sampling for a sufficient number of days during each year. Guided by the explications of *Chapman and Lindzen* [1970] in their section 2L.8, we imposed a criterion of at least three well-distributed samples over 24 h to equip an arbitrary observational day in a 2° box with a "high-frequency" tag. Accumulating these days at each location yielded scatterplots that are exemplified in Figure 7 and reminiscent of major shipping routes in 1900 and 1910 prior to the opening of the Panama Canal in the year 1914. Only a limited amount of 2° boxes feature subdaily observations for more than 40 days, but these statistics increase drastically (>100 days) when the pressure data are grouped to 3° or larger cell sizes. Hence, the ICOADS sampling across synoptic spatial scales is sufficient to map the lunar barometric tide into the analysis system. Note also that the static ocean tide contribution δp_{M_2} off the coast of Brazil is of large magnitude (>50 μbar, Figure 1b) and mostly in phase with the dynamic L_2 component. Even though this lifting term is inconsistent with the notion of a crust-referred tide, it likely provides some of the early excitation of L_2 in ERA-20C.

Proceeding from these findings, we also assume that distinct changes in the ICOADS network must have a repercussion on the appearance of the lunar pressure tide. In particular, marine data around South America are exceedingly sparse during World War I (Figure 7), and one would therefore expect the L_2 wave in that region to fade away. Accordingly, we analyzed the temporal evolution of the semidiurnal lunar tide over the period 1900–1930 in a rectangular domain bounded by 45°N–45°S and 85°W–20°W, which corresponds to the extension of the South American maximum in Figure 6. Yearly solutions of the global L_2 tide were computed in 3 year sliding windows, and their signal-to-noise ratio was further increased by transforming the gridded harmonics to the latitude versus wavenumber domain and retaining only the main modes of wavenumber $|s| \leq 3$ in the inverse transform. Tidal components in the above-noted rectangular box were

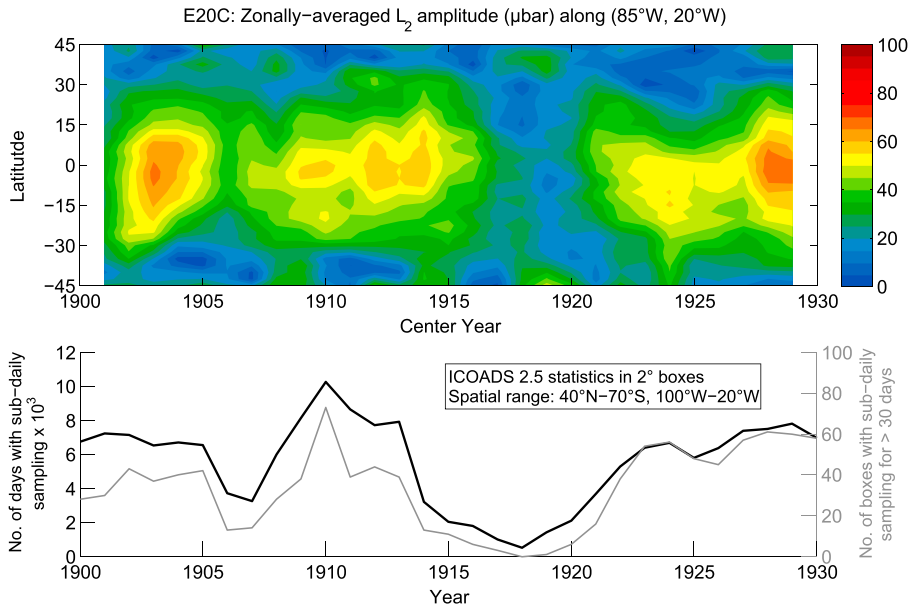

Figure 8. Evolution of the regional L_2 signal in ERA-20C across Middle/South America (domain: 45°N–45°S/85°W–20°W) in the early twentieth century as a function of the changing observational network. Yearly solutions of the global L_2 wave were successively computed in 3 year averaging periods and subject to wavenumber filtering. The zonally averaged tidal amplitude in μbar along (top) 85°W–20°W is juxtaposed to yearly pressure data statistics from (bottom) 2° ocean boxes. The gray curve displays the number of boxes with subdaily sampling for at least 30 days, while the black curve measures the total number of high-frequency days as accumulated from all available boxes in each year.

then condensed to zonal averages in each year and are depicted in terms of amplitude in Figure 8 together with ICOADS pressure data statistics from 2° boxes. In detail, the yearly scatterplots in the manner of Figure 7 were collapsed to the number of boxes with subdaily sampling for more than 30 days as well as to the total count of high-frequency days. The availability of these data clearly impinges on the strength of the L_2 wave that almost vanishes at the end of World War I. By contrast, a rather stable network of observations, visible for instance from 1900 to 1905 or from 1923 onward, correlates well with tidal peak amplitudes of about 50 μbar.

6. Summary Remarks

Our validation of the barometric L_2 tide in ERA-Interim and ERA-20C against an empirical reference model has testified to the overall credibility of these reanalyses in describing the lunar gravitational oscillation in the atmosphere. A completely adequate representation of the tide is, however, impaired by the omission of the respective forcing mechanisms in the physical model equations and the use of an invariant lower atmospheric boundary over both land and water surfaces, which results in large local ocean tide artifacts. Thus, despite the tempting availability of reanalysis fields on a global three-dimensional grid, users from the aeronomy community should exercise caution when deploying ERA-Interim-based tidal solutions as a lower boundary condition for their numerical experiments.

This study also has gone some way toward updating the previous ground truth model of *Haurwitz and Cowley* [1969] and thereby refining our knowledge of L_2 down to regional scales. In particular, the underrepresentation of nonmigrating modes compared to the main wavenumber $s=2$ component in the Haurwitz and Cowley data set [*Vial and Forbes*, 1994] has been amended, and zonal interruptions in the tidal amplitude are now well in accordance with the results from numerical simulations. Using our updated empirical model for a renewed assessment of the L_2 contribution to the planetary M_2 dissipation rate [*Platzman*, 1991; *Ray et al.*, 2001] is an appealing prospect, even though the changes with respect to published dissipation values can be expected to be only marginally significant.

Moreover, we recall that GRACE monthly mean gravity fields are corrected for short-period atmospheric mass variations based on 6-hourly atmospheric data from either operational analyses or reanalyses of the ECMWF [*Fagiolini et al.*, 2015; *Forootan et al.*, 2014]. Other high-frequency periodic signals, related, e.g., to solid Earth

and ocean tides, are routinely removed from the GRACE sensor data by means of separate background models for each of the relevant frequencies, and one might proceed in a similar manner for lunar tidal variations in the atmosphere. We suggest to remove the L_2 signal in ECMWF pressure fields prior to the integration of the 6-hourly atmospheric background model [*Flechtner and Dobslaw*, 2013] and apply an individual correction data set for the lunar atmospheric tide based on the empirical L_2 account presented in this study.

Acknowledgments

Thanks are owed to Tsubasa Kohyama and two anonymous reviewers for evaluating this manuscript. We acknowledge valuable presubmission comments from David Salstein and are grateful to Richard Ray for supplying his own comprehensive L_2 compilation that served as a reference data set throughout this work. Scott Woodruff and Steven Worley kindly allowed us to reprint some of the ICOADS Release 2.5 coverage maps. Financial support of this study was made available by the Austrian Science Fund (FWF) and the Deutsche Forschungsgemeinschaft (DFG) within project I1479-N29. We also thank Deutscher Wetterdienst, Offenbach, Germany, and appreciate the provision of meteorological data by the ECMWF, Reading, U.K., the National Centers of Environmental Information (NOAA), U.S., and the Research Data Archive (RDA) of NCAR, U.S. *Data availability.* The in situ tidal estimates and the gridded empirical L_2 model for the annual mean and the three seasons can be downloaded at http://ggosatm.hg.tuwien.ac.at/L2.html.

References

Carrère, L., F. Lyard, M. Cancet, A. Guiloot, and L. Roblou (2012), FES 2012: A new global tidal model taking advantage of nearly 20 years of altimetry, paper presented at The Symposium 20 Years of Progress in Radar Altimetry, ESA SP, Venice, Italy, 24–29 Sept.

Cartwright, D. E. (1999), *Tides: A Scientific History*, Cambridge Univ. Press, Cambridge, U. K.

Chapman, S., and R. S. Lindzen (1970), *Atmospheric Tides*, D. Reidel, Dordrecht, Netherlands.

Covey, C., A. Dai, D. Marsh, and R. S. Lindzen (2011), The surface pressure signature of atmospheric tides in modern climate models, *J. Atmos. Sci.*, *68*, 495–514, doi:10.1175/2010JAS3560.1.

Cram, T. A., et al. (2015), The International Surface Pressure Databank, version 2, *Geosci. Data J.*, *2*, 31–46, doi:10.1002/gdj3.25.

Dee, D. P., et al. (2011), The ERA-Interim reanalysis: Configuration and performance of the data assimilation system, *Q. J. R. Meteorol. Soc.*, *137*, 553–597, doi:10.1002/qj.828.

Dill, R., and H. Dobslaw (2013), Numerical simulations of global-scale high-resolution hydrological crustal deformations, *J. Geophys. Res. Solid Earth*, *118*, 5008–5017, doi:10.1002/jgrb.50353.

Egbert, G. D., and S. Y. Erofeeva (2002), Efficient inverse modeling of barotropic ocean tides, *J. Atmos. Ocean. Technol.*, *19*, 183–204.

Fagiolini, E., F. Flechtner, M. Horwath, and H. Dobslaw (2015), Correction of inconsistencies in ECMWF's operational analysis data during de-aliasing of GRACE gravity models, *Geophys. J. Int.*, *202*, 2150–2158, doi:10.1093/gji/ggv276.

Flechtner, F., and H. Dobslaw (2013), GRACE AOD1B product description document for product release 05, GRACE Document 327-750, Rev. 4.0, GeoForschungsZentrum Potsdam, Potsdam, Germany.

Forbes, J. M., and X. Zhang (2012), Lunar tide amplification during the January 2009 stratosphere warming event: Observations and theory, *J. Geophys. Res.*, *117*, A12312, doi:10.1029/2012JA017963.

Forbes, J. M., X. Zhang, S. Bruinsma, and J. Oberheide (2013), Lunar semidiurnal tide in the thermosphere under solar minimum conditions, *J. Geophys. Res. Space Physics*, *118*, 1788–1801, doi:10.1029/2012JA017962.

Forootan, E., O. Didova, M. Schumacher, J. Kusche, and B. Elsaka (2014), Comparisons of atmospheric mass variations derived from ECMWF reanalysis and operational fields, over 2003–2011, *J. Geod.*, *88*, 503–514, doi:10.1007/s00190-014-0696-x.

Goulter, S. W. (2005), The structure of the lunar semi-diurnal pressure tide L2, *Q. J. R. Meteorol. Soc.*, *131*, 723–758, doi:10.1256/qj.03.234.

Hamilton, K., S. C. Ryan, and W. Ohfuchi (2008), Topographic effects on the solar semidiurnal surface tide simulated in a very fine resolution general circulation model, *J. Geophys. Res.*, *113*, D17114, doi:10.1029/2008JD010115.

Haurwitz, B., and A. D. Cowley (1969), The lunar barometric tide, its global distribution and annual variation, *Pure Appl. Geophys.*, *77*, 122–150, doi:10.1007/BF00876008.

Hersbach, H., C. Peubey, A. Simmons, P. Berrisford, P. Poli, and D. Dee (2015), ERA-20CM: A twentieth-century atmospheric model ensemble, *Q. J. R. Meteorol. Soc.*, *141*, 2350–2375, doi:10.1002/qj.2528.

Hollingsworth, A. (1971), The effect of ocean and Earth tides on the semi-diurnal lunar air tide, *J. Atmos. Sci.*, *28*, 1021–1044.

Janssen, P. A. E. M. (1999), On tides in the ECMWF model, Tech. Memo. 284, European Centre for Medium-Range Weather Forecasts, Reading, U. K.

Kohyama, T., and J. M. Wallace (2014), Lunar gravitational atmospheric tide, surface to 50 km in a global, gridded data set, *Geophys. Res. Lett.*, *41*, 8660–8665, doi:10.1002/2014GL060818.

Lott, J. N. (2004), The quality control of the Integrated Surface Hourly Database, paper presented at the 14th Conference on Applied Climatology, Am. Meteorol. Soc., Seattle, Wash., 10–16 Jan.

Mass, C. F., W. J. Steenburgh, and D. M. Schultz (1991), Diurnal surface-pressure variations over the continental United States and the influence of sea level reduction, *Mon. Weather Rev.*, *119*, 2814–2830.

McPhaden, M. J., et al. (2010), The Global Tropical Moored Buoy Array, in *Proceedings of the OceanObs'09: Sustained Ocean Observations and Information for Society Conference*, vol. 2, edited by J. Hall, D. E. Harrison, and D. Stammer, ESA Publ. WPP-306, Venice, Italy.

Miyahara, S. (1972), The Earth tide correction for the surface barometric lunar tide, *J. Meteorol. Soc. Jpn.*, *50*, 342–345.

Newton, I. (1687), *Philosophiae Naturalis Principia Mathematica*, Joseph Streater, London.

Nuss, W. A., and D. W. Titley (1994), Use of multiquadric interpolation for meteorological objective analysis, *Mon. Weather Rev.*, *122*, 1611–1631.

Padman, L., and S. Erofeeva (2005), Tide Model Driver (TMD) Manual, Version 1.2. Earth and Space Research, Seattle, Wash. [Available at www.esr.org/polar_tide_models/README_TMD.pdf, last accessed 21 January 2015.]

Pedatella, N. M., H.-L. Liu, and A. D. Richmond (2012), Atmospheric semidiurnal lunar tide climatology simulated by the Whole Atmosphere Community Climate Model, *J. Geophys. Res.*, *117*, A06327, doi:10.1029/2012JA017792.

Petit, G., and B. Luzum (2010), IERS Conventions, IERS Tech. Note 36, Verlag des Bundesamts für Kartographie und Geodäsie, Frankfurt am Main, Germany.

Platzman, G. W. (1988), The atmospheric tide as a continuous spectrum: Lunar semidiurnal tide in surface pressure, *Meteorol. Atmos. Phys.*, *38*, 70–88, doi:10.1007/BF01029949.

Platzman, G. W. (1991), An observational study of energy balance in the atmospheric lunar tide, *Pure Appl. Geophys.*, *137*, 1–33, doi:10.1007/BF00876887.

Poli, P., et al. (2013), The data assimilation system and initial performance evaluation of the ECMWF pilot reanalysis of the 20th-century assimilating surface observations only (ERA-20C), ERA Rep. Ser., 14, European Centre for Medium-Range Weather Forecasts, Reading, U. K.

Pugh, D. T., and P. L. Woodworth (2014), *Sea-Level Science: Understanding Tides, Surges, Tsunamis and Mean Sea-Level Changes*, Cambridge Univ. Press, Cambridge, U. K.

Ray, R. D. (1998), Diurnal oscillations in atmospheric pressure at twenty-five small oceanic islands, *Geophys. Res. Lett.*, *25*, 3851–3854, doi:10.1029/1998GL900039.

Ray, R. D. (2001), Comparisons of global analyses and station observations of the S_2 barometric tide, *J. Atmos. Sol. Terr. Phys.*, *63*, 1085–1097, doi:10.1016/S1364-6826(01)00018-9.

Ray, R. D., R. J. Eanes, and F. G. Lemoine (2001), Constraints on energy dissipation in the Earth's body tide from satellite tracking and altimetry, *Geophys. J. Int.*, *144*, 471–480, doi:10.1046/j.1365-246x.2001.00356.x.

Sabine, E. (1847), On the lunar atmospheric tide at St. Helena, *Philos. Trans. R. Soc. London*, *137*, 45–50.

Schindelegger, M., and R. D. Ray (2014), Surface pressure tide climatologies deduced from a quality-controlled network of barometric observations, *Mon. Weather Rev.*, *142*, 4872–4889.

Smith, A., N. Lott, and R. Vose (2011), The Integrated Surface Database: Recent developments and partnerships, *Bull. Am. Meteorol. Soc.*, *92*, 704–708, doi:10.1175/2011BAMS3015.1.

Stening, R. J., J. M. Forbes, M. E. Hagan, and A. D. Richmond (1997), Experiments with a lunar atmospheric tidal model, *J. Geophys. Res.*, *102*(D12), 13,465–13,471, doi:10.1029/97JD00778.

Tapley, B. D., S. Bettadpur, M. Watkins, and C. Reigber (2004), The gravity recovery and climate experiment: Mission overview and early results, *Geophys. Res. Lett.*, *31*, L09607, doi:10.1029/2004GL019920.

Vial, F., and J. M. Forbes (1994), Monthly simulations of the lunar semi-diurnal tide, *J. Atmos. Terr. Phys.*, *56*, 1591–1607.

Woodruff, S. D., et al. (2011), ICOADS Release 2.5: Extensions and enhancements to the surface marine meteorological archive, *Int. J. Climatol.*, *31*, 951–967, doi:10.1002/joc.2103.